scientific reports

Check for updates

OPEN

Superatomic icosahedral-C_nB_{12-n} (n = 0, 1, 2) Stuffed mononuclear and binuclear borafullerene and borospherene nanoclusters with spherical aromaticity

Min Zhang, Wei-Ping Jia, Ting Zhang, Bin-Bin Pei, Jia Xu, Xinxin Tian, Hai-Gang Lu✉ & Si-Dian Li✉

Boron and boron-based nanoclusters exhibit unique structural and bonding patterns in chemistry. Extensive density functional theory calculations performed in this work predict the mononuclear walnut-like C_i $C_{50}B_{54}$ (1) (C_2B_{10}@$C_{48}B_{44}$), C_1 $C_{50}B_{54}$ (2) (CB_{11}@$C_{49}B_{43}$), and S_{10} $C_{50}B_{54}$ (3) (B_{12}@$C_{50}B_{42}$) which contain one icosahedral-C_nB_{12-n} core (n = 0, 1, 2) at the center following the Wade's skeletal electron counting rules and the approximately electron sufficient binuclear peanut-like C_s $C_{88}B_{78}$ (4) ((C_2B_{10})$_2$@$C_{84}B_{58}$), C_s $C_{88}B_{78}$ (5) ((CB_{11})$_2$@$C_{86}B_{56}$), C_s $C_{88}B_{78}$ (6) ((B_{12})$_2$@$C_{88}B_{54}$), C_s B_{180} (7) ((B_{12})$_2$@B_{156}), C_s B_{182} (8) ((B_{12})$_2$@B_{158}), and C_s B_{184} (9) ((B_{12})$_2$@B_{160}) which encapsulate two interconnected C_nB_{12-n} icosahedrons inside. These novel core–shell borafullerene and borospherene nanoclusters appear to be the most stable species in thermodynamics in the corresponding cluster size ranges reported to date. Detailed bonding analyses indicate that the icosahedral B_{12}^{2-}, CB_{11}^{-}, and C_2B_{10} cores in these core–shell structures possess the superatomic electronic configuration of $1S^21P^61D^{10}1F^8$, rendering spherical aromaticity and extra stability to the systems. Such superatomic icosahedral-C_nB_{12-n} stuffed borafullerenes and borospherenes with spherical aromaticity may serve as embryos to form bulk boron allotropes and their carbon-boron binary counterparts in bottom-up approaches.

Boron ($1s^22s^22p^1$) exhibits unique structures and bonding patterns in chemistry to compensate for its prototypical electron-deficiency[1]. Dicoordinated boranes and tricoordinated borylenes are found to possess special reactivities on dinitrogen (N_2) activations in both recent experimental and theoretical investigations[2–4]. At least sixteen distinct bulk boron allotropes have been experimentally known to be predominately constructed by interconnected icosahedral-B_{12} cages that in many cases are accompanied by interstitial boron atoms lying outside the icosahedrons, the most widely accepted structural model of boron-rich boron carbide B_4C has CB_{11} icosahedrons with C-B-C intericosahedral chains, while the most frequently encountered boranes and carboranes contain icosahedral-C_nB_{12-n} skeletons (n = 0, 1, 2)[1,5–8]. Derivatives of icosahedral borane $B_{12}H_{12}^{2-}$ and carborane $C_2B_{10}H_{12}$ bound to tumor-specific antigens have been the main focus of interests in the area of boron neutron capture therapy (BNCT)[1] and globular $B_{12}Br_{12}^{2-}$ was recently found to function as anionic inorganic membrane carriers for a broad range of hydrophilic cargo molecules[9], further indicating the importance of *closo*-C_nB_{12-n} icosahedrons in boron chemistry and materials science. In contrast, persistent joint photoelectron spectroscopy (PES) and first-principles theory investigations in the past two decades have shown that size-selected $B_n^{-/0}$ nanoclusters exhibit a great structural diversity in an unexpectedly wide size range, including the planar or quasi-planar (2D) boron clusters (n = 3–38, 41, 42) which provided experimental evidence for the viability of monolayer borophenes[10–12], cage-like borospherenes D_{2d} $B_{40}^{-/0}$ and C_3/C_2 B_{39}[13,14] which were late extended to the B_n^q borospherene family (n = 36–42, q = n−40) at first-principles theory level[15–18], and bilayer D_{2h} $B_{48}^{-/0}$ which was recently expanded to the bilayer B_{50}–B_{72} series and a bottom-up approach from medium-sized boron nanoclusters to bilayer borophenes at density functional theory (DFT)[19–24]. Seashell-like borospherenes C_2 B_{28}^- and C_s B_{29}^- were observed in PES measurements as minor isomers of the systems[25,26]. Neutral fullerene-like D_{2d} B_{14} and double-ring tubular D_{2d} B_{20} have also been predicted at first-principles theory levels[27,28]. Inspired by the

Institute of Molecular Science, Shanxi University, Taiyuan 030006, China. ✉email: luhg@sxu.edu.cn; lisidian@sxu.edu.cn

previously predicted icosahedral-B_{12} stuffed amorphous B_{74}, B_{84}, B_{101}, and B_{102}[29–32] and based on the structural motif of D_{5h} C_{70} and extensive DFT calculations, our group recently reported the high-symmetry core–shell C_{5v} B_{111}^{+} which satisfies the Wade's $n+1$ and $n+2$ skeletal electron counting rules exactly and the approximately electron sufficient C_s B_{111}, C_s B_{112}, C_s B_{113}, and C_s B_{114} which are the most stable neutral core–shell borospherenes with a superatomic icosahedral-B_{12} core at the center reported to date in the size range between B_{68}-B_{130}, with C_s B_{112} being the thermodynamically most favorite species in the series[33]. The newly proposed high-symmetry core–shell T_h B_{96}[34] appears to be about 0.020 eV atom^{-1} less stable than our C_s B_{112} and C_s B_{113} at DFT. However, core–shell borospherene nanoclusters with more than one B_{12} icosahedrons at the center still remain unknown in both experiments and theory, missing an important step to form bulk boron allotropes from medium-sized boron nanoclusters in bottom-up approaches.

Facile gas-phase formations of cage-like borafullerenes $C_{59}B$ and $C_{69}B$ by atomic exchange resulting from exposure of pristine C_{60} and C_{70} to boron vapor were firstly realized in 2013, with doubly and triply doped molecules, as well as $C_{56}B_4$ and higher doped fullerenes formed at lower abundances, depending on exposure time and the amount of B available for reaction[35]. Meanwhile, theoretical investigations on the structural and electronic properties of the borafullerenes $C_{60-n}B_n$ ($n=1$–12) and core–shell borafullerene $C_{12}B_{68}$ have been reported in the literature[36,37]. Borafullerenes $B_{40}C_{30}$, $B_{40}C_{40}$, and $B_{40}C_{50}$ isovalent with C_{60}, C_{70}, and C_{80}, respectively, have also been predicted at DFT[38]. Prasad and Jemmis considered the stability of core–shell borafullerenes ($C_{50}B_{34}$ and $C_{48}B_{36}^{2-}$) based on Wade's skeletal electron counting rules at DFT level[39]. Nevertheless, the thermodynamically most stable core–shell borafullerene nanoclusters stuffed with one or more than one C_nB_{12-n} icosahedrons ($n=0$, 1, 2) at the center have not been reported to date.

Keeping the inspiration in mind and based on extensive DFT calculations, we predict herein the walnut-like C_i $C_{50}B_{54}$ (**1**) (C_2B_{10}@$C_{48}B_{44}$), C_1 $C_{50}B_{54}$ (**2**) (CB_{11}@$C_{49}B_{43}$), S_{10} $C_{50}B_{54}$ (**3**) (B_{12}@$C_{50}B_{42}$) based on the structural motif of I_h C_{80} which possess one C_nB_{12-n} icosahedron ($n=0$, 1, 2) at the center and the peanut-like C_s $C_{88}B_{78}$ (**4**), C_s $C_{88}B_{78}$ (**5**), C_s $C_{88}B_{78}$ (**6**), C_s B_{180} (**7**), C_s B_{182} (**8**), C_s B_{184} (**9**) which possess two interconnected icosahedral-C_nB_{12-n} cores as the most stable species in the corresponding cluster size ranges reported to date. The icosahedral-C_nB_{12-n} cores ($n=0$, 1, 2) in these core–shell borafullerene and borospherene nanoclusters possess prototypical superatomic electronic configurations, rendering spherical aromaticity and extra stability to the systems.

Computational procedures. Based on the structural motif of I_h C_{80}, we manually constructed the initial structures of the icosahedral-C_nB_{12-n} ($n=0$, 1, 2) stuffed core–shell $C_{50}B_{54}$ clusters which follow the Wade's $n+1$ and $n+2$ skeletal electron counting rules[1] exactly (Fig. S1). However, locating the most stable isomer of such a medium-sized C–B binary cluster with huge numbers of possible positional isomers appeared to be a computationally daunting task. To solve the problem, we compiled the Fixed Motif Local Minimum Search (FMLMS) program in this work which includes random structural generations based on the designated structural motifs, symmetry recognitions using the Symmol code[40], and structural similarity checks using the Ultrafast Shape Recognition (USR) approach[41,42]. Semi-empirical quantum mechanical calculations using the GFNn-xTB program were implemented to optimize the constructed structures from FMLMS initially and screen out the most concerned low-lying isomers, followed by structural optimizations using the CP2K software suite[43–45]. Such a procedure proved to work well in locating the recently reported most stable core–shell borospherenes of B_{111}-B_{114} based on the structural motif of D_{5h} C_{70}[33]. The low-lying isomers of the core–shell $C_{50}B_{34}$, $C_{50}B_{44}$, $C_{50}B_{54}$ and $C_{88}B_{78}$ binary nanoclusters based on the structural motifs of I_h C_{60}, D_{5h} C_{70}, I_h C_{80}, and D_{5d} C_{120}, were located using FMLMS in this work, respectively (Figs. S4, S5 and S7). Similar processes were implemented on the binuclear core–shell C_2 B_{172}, C_s B_{176}, C_2 B_{178}, C_s B_{180}, C_s B_{182}, C_s B_{184}, C_2 B_{186}, C_s B_{188}, C_s B_{190}, C_s B_{192} (Figs. 2b, S8) based on the structural pattern of C_{2v} C_{110} as an extension of the previously reported most stable mononuclear C_s B_{112}[33]. The lowest-lying ten to twenty isomers were then fully optimized at both DFT-PBE0[46] and TPSSh[47] levels with the all-electron basis sets of 6-31G(d) for both C and B[48] implemented in Gaussian 09 suite[49], with the relative energies further refined for the first few competitive lowest-energy isomers at PBE0/6-311G(d)[46–48]. Extensive Born–Oppenheimer molecular dynamics (BOMD) simulations were implemented for 30 ps on C_i $C_{50}B_{54}$ (**1**) and S_{10} $C_{50}B_{54}$ (**3**) at 1500 K and C_s B_{184} (**9**) at 500 K using the CP2K program[45] to verify their dynamic stability at high temperatures. Natural bonding orbital (NBO) analyses were performed using the NBO 6.0 program[50]. Nucleus-independent chemical shifts (NICS)[51,52] were calculated at the centers of the C_nB_{12-n} icosahedrons ($n=0$, 1, 2) to assess the spherical aromaticity of core–shell systems. Detailed bonding analyses on C_i $C_{50}B_{54}$ (**1**), S_{10} $C_{50}B_{54}$ (**3**), C_s $C_{88}B_{78}$ (**4**), C_s B_{182} (**8**) and C_s B_{184} (**9**) were carried out using the adaptive natural density partitioning (AdNDP 2.0) method[53,54] at the PBE0/6-31G level[46,48]. The Electron Density of Delocalized Bonds (EDDB) was calculated using the EDDB code[55,56], with the EDDB isosurfaces generated using the visual molecular dynamics (VMD) software[57] to visualize the distribution of delocalized bonds. The IR and Raman spectra of C_i $C_{50}B_{54}$ (**1**), C_s $C_{88}B_{78}$ (**4**), and C_s B_{184} (**9**) were theoretically simulated at PBE0/6-31G(d).

Results

Structures and stabilities. The structural constructions of mononuclear $C_{50}B_{54}$ (**1, 2, 3**), binuclear C_s $C_{88}B_{78}$ (**4, 5, 6**), and binuclear B_{180} (**7**), B_{182} (**8**), and B_{184} (**9**) starting from the structural motifs of the corresponding fullerenes are illustrated in Figs. S1, S2 and S3, respectively. The optimized core–shell borafullerenes C_i $C_{50}B_{54}$ (**1**) (C_2B_{10}@$C_{48}B_{44}$), C_1 $C_{50}B_{54}$ (**2**) (CB_{11}@$C_{49}B_{43}$), and S_{10} $C_{50}B_{54}$ (**3**) (B_{12}@$C_{50}B_{42}$) with one icosahedral-C_nB_{12-n} ($n=0$, 1, 2) core at the center, core–shell borafullerenes C_s $C_{88}B_{78}$ (**4**) ((C_2B_{10})$_2$@$C_{84}B_{58}$), C_s $C_{88}B_{78}$ (**5**) ((CB_{11})$_2$@$C_{86}B_{56}$), C_s $C_{88}B_{78}$ (**6**) ((B_{12})$_2$@$C_{88}B_{54}$) with two interconnected icosahedral-C_nB_{12-n} ($n=0$, 1, 2) cores, and core–shell borospherenes C_s B_{180} (**7**) ((B_{12})$_2$@B_{156}), C_s B_{182} (**8**) ((B_{12})$_2$@B_{158}), and C_s B_{184} (**9**) ((B_{12})$_2$@B_{160}) with two interconnected icosahedral-B_{12} cores are collectively shown in Fig. 1, with more alternative low-lying isomers obtained for $C_{50}B_{54}$, $C_{88}B_{78}$, and B_{184} depicted in Figs. S4, S5 and S6, respectively.

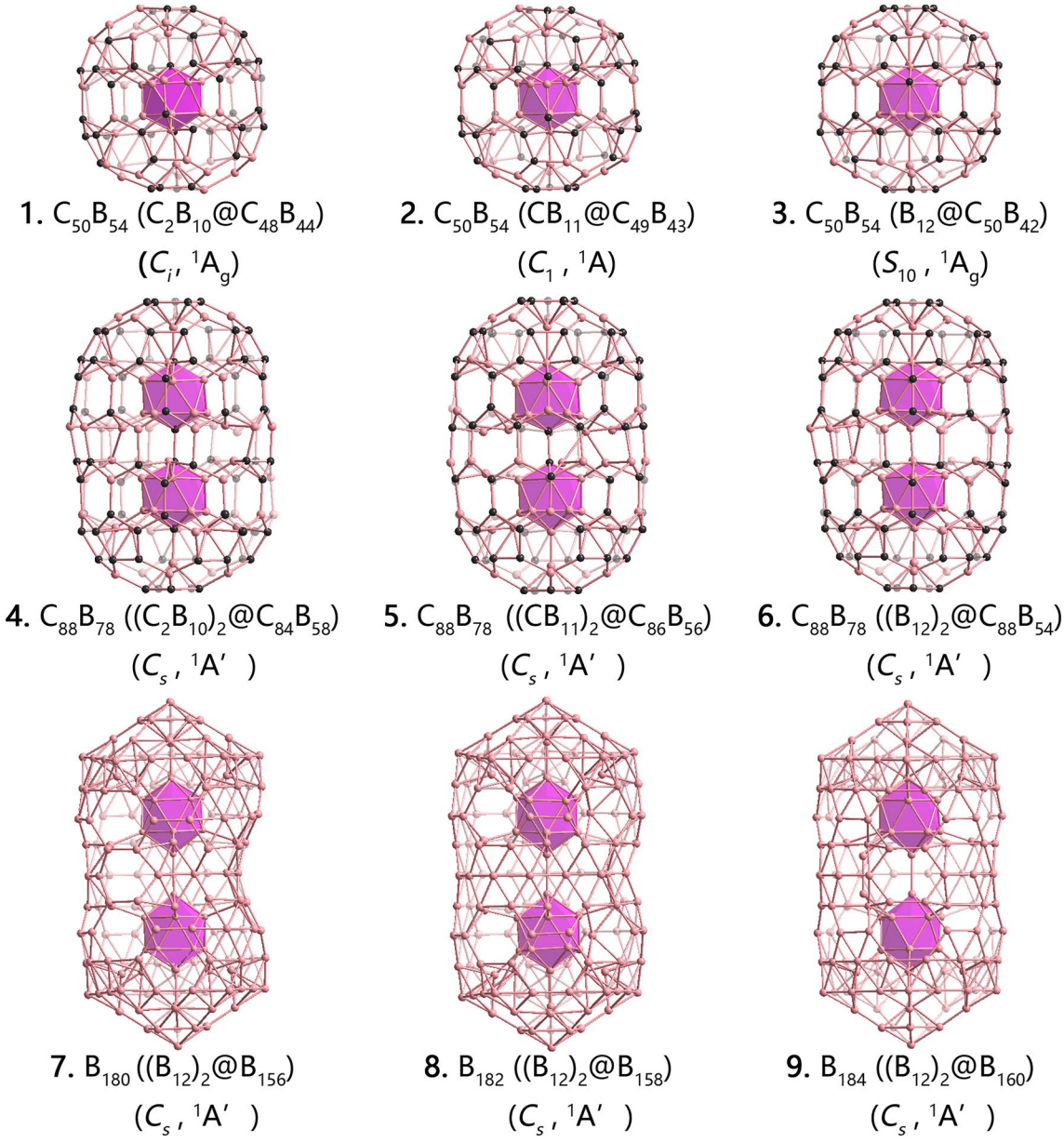

Figure 1. Optimized structures of C_i $C_{50}B_{54}$ (**1**), C_1 $C_{50}B_{54}$ (**2**), S_{10} $C_{50}B_{54}$ (**3**), C_s $C_{88}B_{78}$ (**4**), C_s $C_{88}B_{78}$ (**5**), C_s $C_{88}B_{78}$ (**6**), C_s B_{180} (**7**), C_s B_{182} (**8**), and C_s B_{184} (**9**) at PBE0/6-311G(d) level, with the icosahedral-C_nB_{12-n} ($n = 0$, 1, 2) cores at the centers highlighted in purple.

The calculated formation energies per atom $E_f = (E_t - m\mu_B - n\mu_C)/(m+n)$ for the C_mB_n borafullerenes are diagrammatically shown in Fig. 2a where E_t, $\mu_B = EB_{40}/40$, and $\mu_C = EC_{60}/60$ are the total energy of C_mB_n binary clusters and chemical potentials of the experimentally observed D_{2d} B_{40}[13] and I_h C_{60}, respectively, while the cohesive energies per atom $E_c = (E_t - nE)/n$) for B_n core–shell borospherenes are depicted in Fig. 2b where E is the energy of a free B atom in vacuum. The calculated nucleus-independent chemical shift (NICS) values at the geometric centers of the C_nB_{12-n} ($n = 0$, 1, 2) icosahedral cores of the concerned core–shell borafullerenes and borospherenes and their HOMO–LUMO gaps (ΔE_{gap}) at PBE0/6-311G(d) are comparatively tabulated in Tables S1 and S2.

As shown in Fig. S1, with one *closo*-B_{12} icosahedron located at the center and twelve *nido*-B_6 pentagonal pyramids symmetrically distributed on the cage surface, the high-symmetry core–shell I_h B_{104} (B_{12}@B_{92}) based on the structural motif of I_h C_{80} is deficient by 50 electrons according to the Wade's $n+1$ and $n+2$ skeleton electron counting rules and should therefore not be expected to be stable in thermodynamics[32,39,58]. I_h B_{104} can be made electron sufficient by substitution of 50 B atoms on the cage surface with 50 C atoms. Eighteen such low-lying walnut-like $C_{50}B_{54}$ positional isomers within 1.91 eV were obtained using FMLMS in Fig. S4. The high-symmetry S_{10} $C_{50}B_{54}$ (B_{12}@$C_{50}B_{42}$) (**3**) (Fig. 1) as the ninth lowest-lying isomer possesses an almost ideal *closo*-B_{12} icosahedron at the center, ten *nido*-C_4B_2 pentagonal pyramids symmetrically distributed on the waist, and two *nido*-C_5B pentagonal pyramids on the top and bottom. The core–shell C_1 $C_{50}B_{54}$ (CB_{11}@$C_{49}B_{43}$) (**2**) can be obtained by replacing the central B_{12} core in $C_{50}B_{54}$ (**3**) with a *closo*-CB_{11} icosahedron, with the top *nido*-C_5B

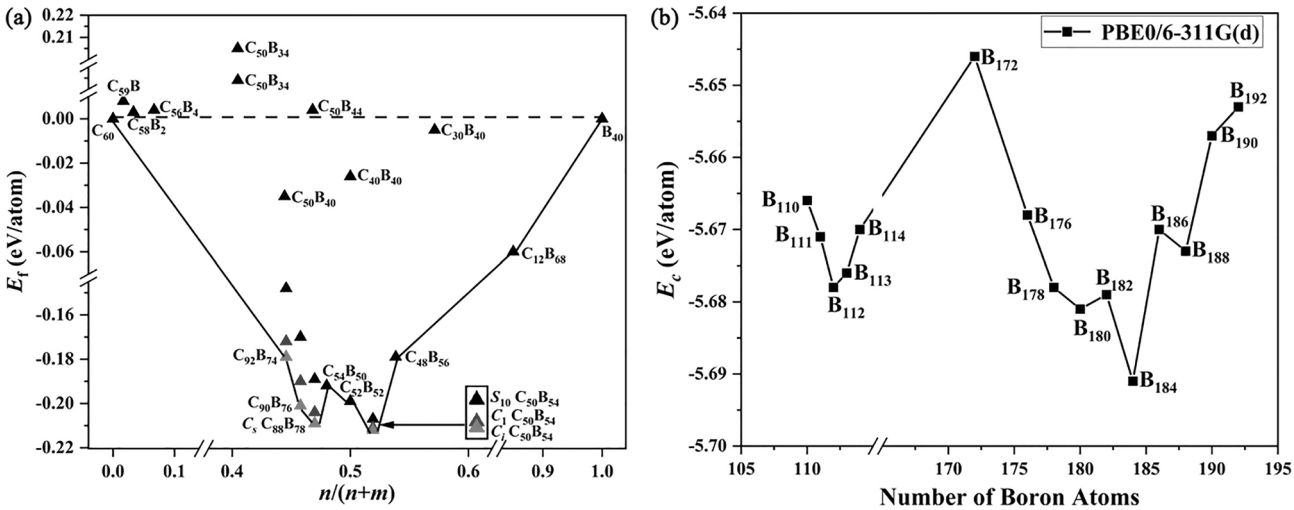

Figure 2. (**a**) Calculated formation energy per atom (E_f, eV atom^{-1}) as a function of the $n/(m+n)$ ratio in the optimized boron–carbon clusters C_mB_n and (**b**) cohesive energy per atom (E_c, eV atom^{-1}) of the optimized core–shell boron clusters B_n (n = 110–192) as a function of the cluster size (n) at PBE0/6-311G(d).

simultaneously changed into a *nido*-C_4B_2 pentagonal pyramid. The most stable $C_{50}B_{54}$ (C_2B_{10}@$C_{48}B_{44}$) (**1**) contains an icosahedral *closo*-C_2B_{10} core at the center and twelve *nido*-C_4B_2 pentagonal pyramids evenly distributed on the cage surface in an overall symmetry of C_i. $C_{50}B_{54}$ (**1**), $C_{50}B_{54}$ (**2**), and $C_{50}B_{54}$ (**3**) prove to be true minima on the potential surface of $C_{50}B_{54}$ with the smallest vibrational frequencies of ν_{min} = 230.2, 222.4, and 208.4 cm^{-1} at PBE0/6-31G(d), respectively.

As shown in Fig. 2a and Table S1, as one of the two local minima on the formation energy $E_f \sim n/(n+m)$ curve, C_i $C_{50}B_{54}$ (**1**) is the most stable core–shell borafullerene obtained to date, with the average formation energy per atom of E_f = − 0.213 eV atom^{-1} with respect to the experimentally known C_{60} and B_{40}. It is 0.11 eV more stable than the second lowest-lying C_1 $C_{50}B_{54}$ (**2**) and 0.58 eV more stable than the ninth lowest-lying S_{10} $C_{50}B_{54}$ (**3**) at PBE0/6-311G(d) level (Fig. S4). Other approximately electron sufficient close-lying species C_i $C_{48}B_{56}$ (B_{12}@$C_{48}B_{44}$), C_2 $C_{52}B_{52}$ (B_{12}@$C_{52}B_{40}$), and C_2 $C_{54}B_{50}$ (B_{12}@$C_{54}B_{38}$) all appear to be obviously less favorable in thermodynamics than C_i $C_{50}B_{54}$ (**1**). The seventeenth high-symmetry isomer C_5 $C_{50}B_{54}$ in the structural motif of D_{5h} C_{80} with a B_{12} icosahedron at the center lies 1.87 eV less stable than $C_{50}B_{54}$ (**1**) (Fig. S1). As indicated in Table S1, $C_{50}B_{54}$ (**1/2/3**) have the largest calculated HOMO–LUMO gaps of ΔE_{gap} = 2.24/2.28/2.75 eV in the low-lying core–shell borafullerene series obtained in this work, well supporting the high chemical stabilities of these mononuclear core–shell borafullerenes. The previously predicted electron sufficient core–shell C_{2h} $C_{50}B_{34}$[39] in the structural motif of I_h C_{60} (which was distorted to a more stable C_1 $C_{50}B_{34}$ obtained in this work, Fig. S7), core–shell C_5 $C_{50}B_{44}$ in the structural motif of D_{5h} C_{70} obtained in this work (Fig. S7), and the previously reported cage-like borafullerenes $C_{30}B_{40}$, $C_{40}B_{40}$, and $C_{50}B_{40}$[38] all appear to be obviously less favorable than $C_{50}B_{54}$ (**1**) (Fig. 2a). It is also noticed that $C_{50}B_{54}$ (**1**), $C_{50}B_{54}$ (**2**), and $C_{50}B_{54}$ (**3**) are all considerably more favorable in formation energies than the experimentally observed $C_{59}B$, $C_{58}B_2$, and $C_{56}B_4$ and theoretically predicted amorphous core–shell C_1 $C_{12}B_{68}$[35–37].

The walnut-like core–shell borafullerenes $C_{50}B_{54}$ (**1**, **2**, **3**) can be extended in axial dimension to form the approximately electron sufficient peanut-like C_s $C_{88}B_{78}$ (**4**) ((C_2B_{10})$_2$@$C_{84}B_{58}$), C_s $C_{88}B_{78}$ (**5**) ((CB_{11})$_2$@$C_{86}B_{56}$), C_s $C_{88}B_{78}$ (**6**) ((B_{12})$_2$@$C_{88}B_{54}$) based on the structural framework of D_{5d} C_{120} which contain two interconnected icosahedral C_2B_{10}, CB_{11}, and B_{12} cores inside the outer shells, respectively (Figs. 1 and S2). C_s $C_{88}B_{78}$ (**4**) as the second local minimum on the $E_f \sim n/(n+m)$ curve (Fig. 2a) with E_f = − 0.209 eV atom^{-1} appears to be 0.005 and 0.020 eV atom^{-1} more stable than $C_{88}B_{78}$ (**5**) and C_s $C_{88}B_{78}$ (**6**) in formation energy, respectively, indicating again that icosahedral-C_2B_{10} cores are better favored in energy over both CB_{11} and B_{12} icosahedrons in core–shell borafullerenes. The electron-precise $C_{92}B_{74}$ and approximately electron sufficient $C_{90}B_{76}$ with two interconnected icosahedral-C_nB_{12-n} cores (n = 0, 1, 2) appear to be slightly less stable in thermodynamics than their $C_{88}B_{78}$ (**4**) counterpart (Fig. 2a). The prediction of mononuclear $C_{50}B_{54}$ (**1**, **2**, **3**) and binuclear $C_{88}B_{78}$ (**4**, **5**, **6**) as the two minima on the $E_f \sim n/(n+m)$ curve indicates that I_h C_{80} and its expanded fullerene analog D_{5d} C_{120} provide the right cavities and optimum structural motifs to form core–shell borafullerenes with one and two icosahedral-C_nB_{12-n} (n = 0, 1, 2) cores (Fig. 2a), respectively. In contrast, the structural motifs generated from both I_h C_{60} and D_{5h} C_{70} appear to be too small in size to host icosahedral-C_nB_{12-n} (n = 0, 1, 2) cores comfortably in core–shell borafullerenes, as demonstrated in the cases of core–shell C_{2h}/C_1 $C_{50}B_{34}$ and C_5 $C_{50}B_{44}$ (Figs. 2a and S7).

As an extension of the previously reported most stable mononuclear C_s B_{112} based on the framework of D_{5h} C_{70}[33], a series of binuclear core–shell borospherenes B_{172}-B_{192} with two interconnected B_{12} icosahedrons at the center based on the structural motif of C_{2v} C_{110} are obtained in this work (Figs. 2b and S3). The almost electron-sufficient C_s B_{188} with the cohesive energy of E_c = − 5.673 eV atom^{-1} (Table S2) appears to be a local minimum on the $E_c \sim n$ curve, but it is obviously less stable in thermodynamics than the approximately electron-sufficient C_s B_{180} (**7**) ((B_{12})$_2$@B_{156}), C_s B_{182} (**8**) ((B_{12})$_2$@B_{158}), and C_s B_{184} (**9**) ((B_{12})$_2$@B_{160}) which all lie within a deeper local minimum with E_c = − 5.681, − 5.679, and − 5.691 eV atom^{-1} at PBE0, respectively (Fig. 2b and

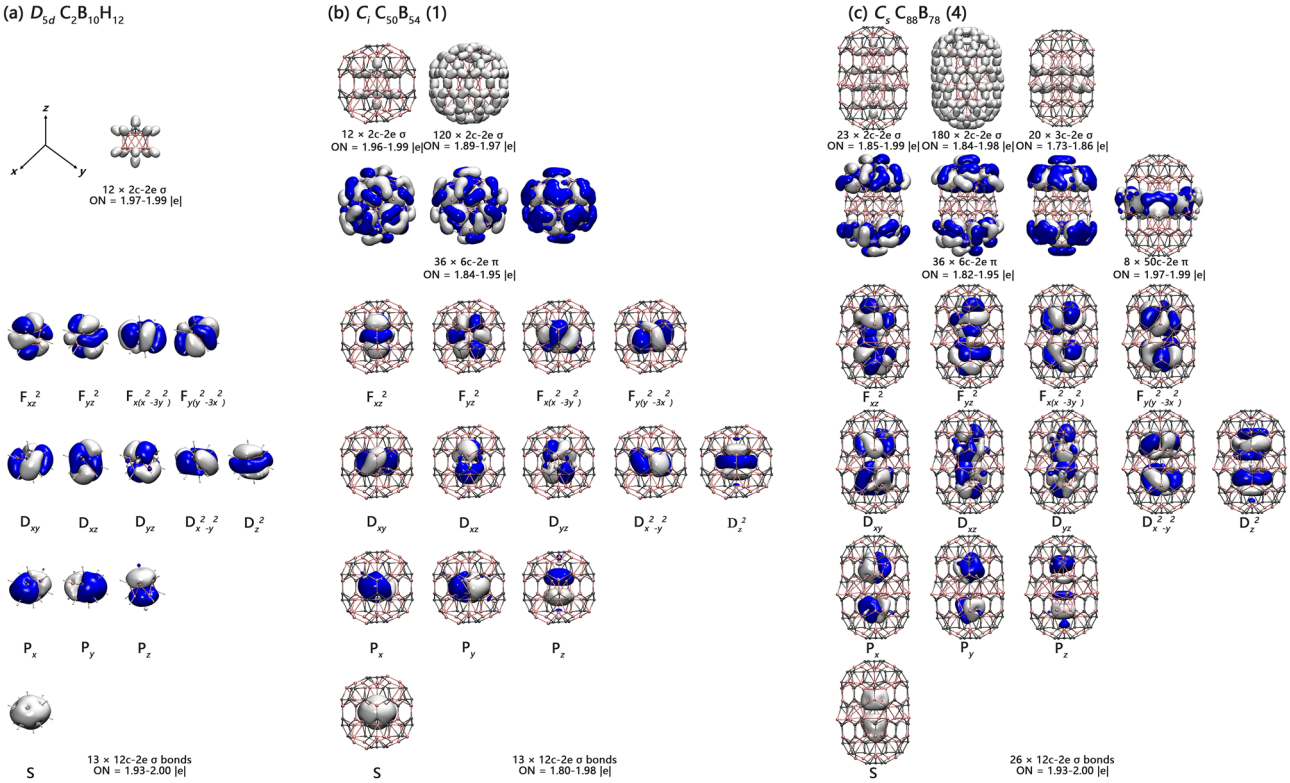

Figure 3. AdNDP bonding patterns of (**a**) D_{5d} $C_2B_{10}H_{12}$, (**b**) C_i $C_{50}B_{54}$ (**1**), and (**c**) C_s $C_{88}B_{78}$ (**4**) with the occupation numbers (ONs) indicated.

Table S2). C_s B_{184} (**9**) as the most stable species on the $E_c \sim n$ curve contains two *closo*-B_{12} icosahedral cores doubly bound to an interstitial B_2 unit. It is even more stable than the previously reported mononuclear C_s B_{112} where $E_c = -5.678$ eV atom^{-1} at the same theoretical level[33]. Similar results are obtained at TPSSh/6-311G(d) in Fig. S8 where C_s B_{184} also appears to be the most stable species in cohesive energy in the size range between B_{110} and B_{192}. Binuclear B_{184} (**9**) with two icosahedral-B_{12} cores and one interstitial B_2 unit is therefore the most stable core–shell borospherene reported to date in thermodynamics.

Extensive BOMD simulations provide strong evidence to support the dynamic stability of these core–shell nanoclusters. As demonstrations in Fig. S9, the thermodynamically stable C_i $C_{50}B_{54}$ (**1**), S_{10} $C_{50}B_{54}$ (**3**), and C_s B_{184} (**9**) were highly dynamically stable at 1500 K, 1500 K, and 500 K, with the small calculated average root-mean-square-deviations of RMSD = 0.10, 0.10, 0.07 Å and maximum bond length deviations of MAXD = 0.37, 0.34, and 0.31 Å, respectively. No other low-lying isomers were observed during the dynamical simulations in 30 ps.

Bonding pattern analyses. The high stability of these core–shell nanoclusters originates from their unique electronic structures and bonding patterns. As demonstrations, detailed AdNDP bonding analyses on both closed-shell C_i $C_{50}B_{54}$ (**1**) and C_s $C_{88}B_{78}$ (**4**) are presented in Fig. 3. The icosahedral-C_2B_{10} cores in both $C_{50}B_{54}$ (**1**) and $C_{88}B_{78}$ (**4**) are connected to the outer shells through radial B–B and C–B bonding interactions. To better understand the bonding nature of these binary core–shell structures, detailed bonding analysis on the prototypical carborane D_{5d} $C_2B_{10}H_{12}$ is performed in Fig. 3a first. As expected, $C_2B_{10}H_{12}$ possesses 12 2c-2e σ bonds in radial directions perpendicular to the cage surface, including 10 2c-2e B–H σ bonds on the waist and 2 2c-2e C–H σ bonds on the top and bottom with the occupation numbers of ON = 1.97–1.99 |e|. The remaining 26 valence electrons are distributed in 13 12c-2e delocalized bonds over the whole D_{5d} icosahedral-$CB_{10}C$ skeleton with ON = 1.93–2.00 |e|, including 1 12c-2e S-type bond, 3 12c-2e P-type bonds, 5 12c-2e D-type bonds, and 4 12c-2e F-type bonds. Such a bonding pattern well corresponds to the superatomic electronic configuration $1S^21P^61D^{10}1F^8$ of D_{5d} $C_2B_{10}H_{12}$ (Fig. S10) which is spherically aromatic in nature, as evidenced by the negative calculated NICS = − 29.22 ppm at the cage center.

The bonding pattern of C_i $C_{50}B_{54}$ (**1**) in Fig. 3b well demonstrates the superatomic behavior of its C_i icosahedral-$CB_{10}C$ core. $C_{50}B_{54}$ (**1**) contains 10 2c-2e B–B bonds and 2 2c-2e C–B σ bonds in radial directions between the $CB_{10}C$ icosahedron and outer shell to saturate the dangling valences of icosahedral core, 120 B-B or B-C or C–C 2c-2e σ bonds on the cage surface, and 36 6c-2e π bonds on 12 *nido*-C_4B_2 pentagonal pyramids in the first row, with 3 6c-2e π bonds over each C_4B_2 pentagonal pyramid matching the $4n + 2$ aromatic rule with $n = 1$ (suggesting the existence of local π-aromaticity over each C_4B_2 pentagon in on the surface of $C_{50}B_{54}$ (**1**), similar to the situation in benzene C_6H_6). Its remaining 13 12c-2e bonds are delocalized over the whole *closo*-$CB_{10}C$ icosahedral core, including 1 12c-2e S-type bond, 3 12c-2e P-type bonds, 5 12c-2e D-type bonds, and 4 12c-2e F-type bonds, well corresponding to the 13 12c-2e delocalized bonds of D_{5d} $C_2B_{10}H_{12}$ in Fig. 3a. Such a bonding pattern clearly indicates that the icosahedral-$CB_{10}C$ core in C_i $C_{50}B_{54}$ (**1**) possesses a typical superatomic electron configuration,

similar to the situation in D_{5d} $C_2B_{10}H_{12}$. Similar bonding patterns exist in C_1 $C_{50}B_{54}$ (**2**) and S_{10} $C_{50}B_{54}$ (**3**) which contain negatively charged icosahedral-CB_{11}^- and icosahedral-B_{12}^{2-} cores, respectively (Fig. S11). The binuclear C_s $C_{88}B_{78}$ (**4**) possesses a similar but more complicated bonding pattern. As shown in Fig. 3c, $C_{88}B_{78}$ (**4**) contains 1 C–C 2c-2e σ bond between the two icosahedral-$CB_{10}C$ cores and 22 B-B or 2 C-B σ bonds in radial directions, 180 B-B or C-B or C–C 2c-2e σ bonds on the cage surface, and 20 3c-2e σ bonds on the waist between ten capping B atoms and the corresponding hexagonal holes on the surface in an overall symmetry of C_s. In addition to the 36 6c-2e π bonds over 12 C_5B or C_4B_2 pentagonal pyramids on the top and bottom, $C_{88}B_{78}$ (**4**) also possesses 8 50c-2e π bonds delocalized over the "girdle" composed of ten hexagonal pyramids on the waist in between. Most interestingly, with 26 12c-2e bonds over the $CB_{10}C$-$CB_{10}C$ binuclear core in $C_{88}B_{78}$ (**4**), there exist 13 12c-2e bonds over each *closo*-$CB_{10}C$ icosahedron, including 1 12c-2e S-type bond, 3 12c-2e P-type bonds, 5 12c-2e D-type bonds, 4 12c-2e F-type bonds, well corresponding to the 13 12c-2e delocalized bonds of D_{5d} $C_2B_{10}H_{12}$ in Fig. 3a. Thus, each *closo*-$CB_{10}C$ icosahedron in $C_{88}B_{78}$ (**4**) follows the superatomic electronic configuration of $1S^21P^61D^{10}1F^8$, corresponding again to the 13 12c-2e delocalized bonds of D_{5d} $C_2B_{10}H_{12}$ in Fig. 3a.

The local π-aromaticities over the twelve C_4B_2 pentagons and spherical aromaticities over each C_2B_{10} icosahedral core in both $C_{50}B_{54}$ (**1**) and $C_{88}B_{78}$ (**4**) are also demonstrated in their calculated EDDB isosurface maps depicted in Fig. S13. The average values of atomic contribution of EDDB = 1.31, 1.33 *e* in the C_2B_{10} icosahedrons in $C_{50}B_{54}$ (**1**) and $C_{88}B_{78}$ (**4**) are obviously larger than the corresponding values of EDDB = 0.93 and 1.00 *e* in the remaining parts, respectively, well supporting the spherical aromaticity of superatomic cores, while the observed high EDDB values over each C_4B_2 pentagon on the cage surface in continuous distributions indicate the existence of local π-aromaticity in the systems.

Such bonding patterns render spherical aromaticity to both C_i $C_{50}B_{54}$ (**1**) and C_s $C_{88}B_{78}$ (**4**), as evidenced by the negative calculated NICS = − 23.23 ppm and NICS = − 32.47, − 28.04 ppm at the cage centers of their C_2B_{10} icosahedral cores, respectively. With the calculated NICS = − 17.70 ppm and NICS = − 32.68, − 32.65 ppm at the cage centers of their C_2B_{10} and B_{12}^{2-} icosahedral cores, respectively, both $C_{50}B_{54}$ (**3**) and B_{184} (**9**) also appear to be spherically aromatic in nature. Similar NICS values exist in the spherically aromatic $C_{50}B_{54}$ (**2**), $C_{50}B_{54}$ (**3**), $C_{88}B_{78}$ (**5**), C_s $C_{88}B_{78}$ (**6**), B_{180} (**7**), and B_{182} (**8**).

IR and Raman spectral simulations. The infrared (IR) and Raman spectra of C_i $C_{50}B_{54}$ (**1**) and C_s $C_{88}B_{78}$ (**4**) are computationally simulated at PBE0/6-31G(d) in Fig. 4 to facilitate their spectral characterizations. C_i $C_{50}B_{54}$ (**1**) exhibits three major IR peaks at 640 (a_u), 1026 (a_u), and 1294 cm^{-1} (a_u), while C_s $C_{88}B_{78}$ (**4**) possesses two major IR peaks at 1234 (a") and 1391 cm^{-1} (a'), respectively. The three major Raman active peaks of $C_{50}B_{54}$ (**1**) occur at 383 (a_g), 1152 cm^{-1} (a_g), and 1405 cm^{-1} (a_g), with the weak peak at 242 cm^{-1} (a_g), strong peaks at 383 (a_g), and strong peak at 1405 cm^{-1} (a_g) representing typical "radial breathing modes" (RBMs) of the outer shell, the core + shell system as a whole, and the inner icosahedral-C_2B_{10} core of C_i $C_{50}B_{54}$ (**1**), respectively. Such RBMs can be used to characterize the hollow boron-based nanostructures in experiments[59]. Similarly, C_s $C_{88}B_{78}$ (**4**) exhibits two major Raman peaks at 1264 cm^{-1} (a') and 1360 cm^{-1} (a') and three RBM vibrational modes at 211 cm^{-1} (a'), 329 cm^{-1} (a'), 858 cm^{-1} (a'), respectively.

Conclusions

The analyses above indicate that, based on the structural motifs of the related fullerenes and extensive DFT calculations, the mononuclear $C_{50}B_{54}$ (**1**, **2**, **3**) and binuclear C_s $C_{88}B_{78}$ (**4**, **5**, **6**), B_{180} (**7**), B_{182} (**8**), and B_{184} (**9**) nanoclusters obtained in this work with one or two icosahedral-C_nB_{12-n} cores at the center are the most stable core–shell borafullerenes and borosphenrenes in thermodynamics in the corresponding cluster size ranges reported to date. The B_{12}^{2-}, CB_{11}^-, and C_2B_{10} icosahedrons encapsulated in these core–shell nanostructures possess the superatomic electronic configurations ($1S^21P^61D^{10}1F^8$) of the experimentally known icosahedral I_h $B_{12}H_{12}^{2-}$, C_5 $CB_{11}H_{12}^-$, and D_{5d} $C_2B_{10}H_{12}$, respectively, rendering prototypical spherical aromaticity to the systems. Theoretical investigations on core–shell borafullerenes and borospherenes with more than two superatomic icosahedral-C_nB_{12-n} cores accompanied by suitable numbers of interstitial boron atoms are currently in progresses. Experimental investigations are invited to synthesize icosahedral-C_nB_{12-n} stuffed core–shell borafullerenes and borospherenes to form bulk boron allotropes and their carbon-boron binary counterparts with novel electronic and mechanic properties in bottom-up approaches.

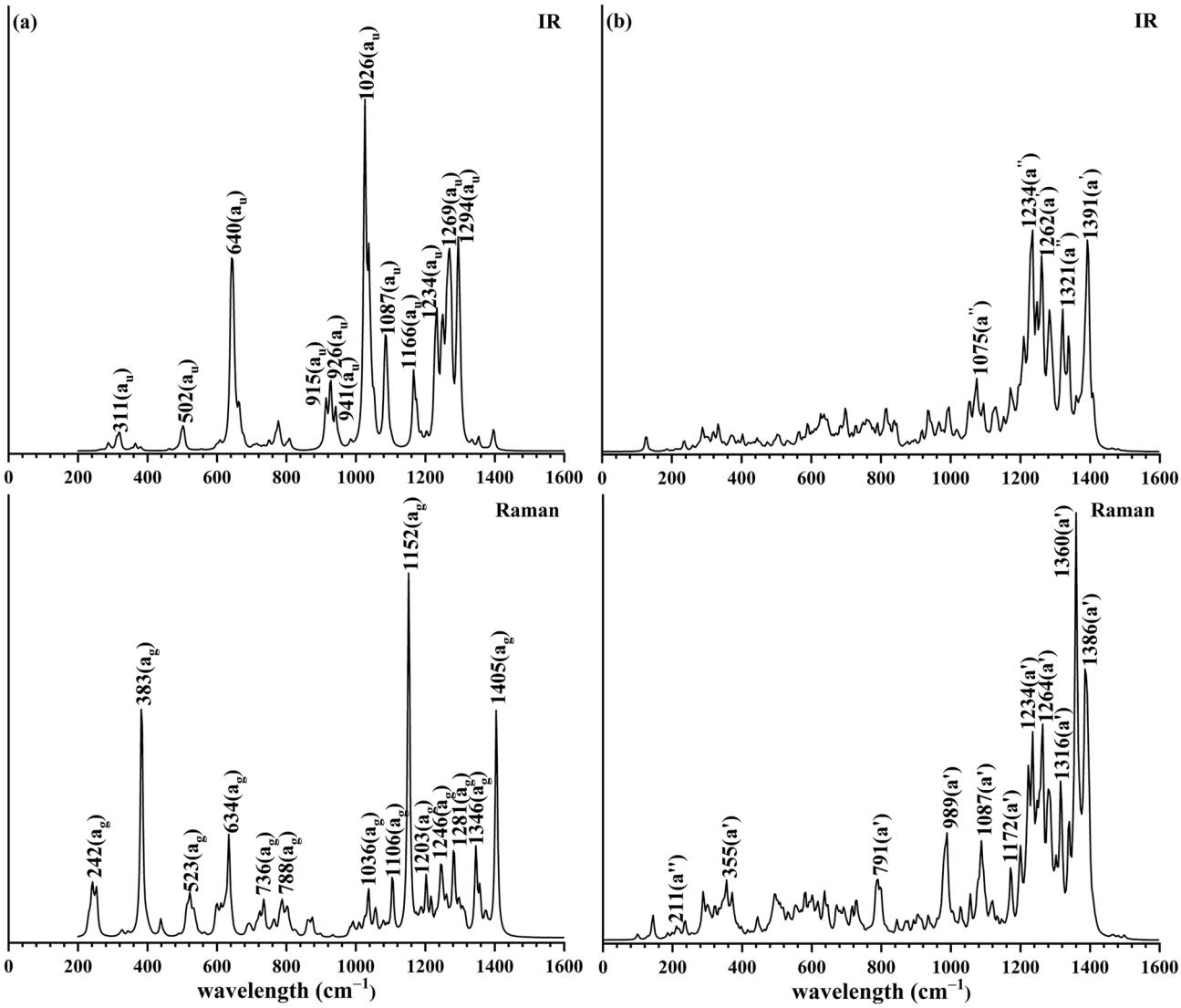

Figure 4. Simulated IR and Raman spectra of (**a**) C_i $C_{50}B_{54}$ (**1**) and (**b**) C_s $C_{88}B_{78}$ (**4**) at PBE0/6-31G(d) level.

Data availability

The datasets used and/or analysed during the current study are available from the corresponding author on reasonable request.

Received: 12 August 2022; Accepted: 4 October 2022
Published online: 17 November 2022

References

1. Cotton, F. A., Wilkinson, G., Murillo, C. A. & Bochmann, M. *Advanced Inorganic Chemistry* 1355 (Wiley-Interscience, New York, 1998).
2. Rouf, A. M., Dai, C. S., Dong, S. C. & Zhu, J. screening borane species for dinitrogen activation. *Inorg. Chem.* **59**, 11770–11781 (2020).
3. Legare, M. A. *et al.* The reductive coupling of dinitrogen. *Science* **363**, 1329–1332 (2019).
4. Rouf, A. M., Dai, C. S., Xu, F. Z. & Zhu, J. Dinitrogen activation by tricoordinated boron species: A systematic design. *Adv. Theory Simul.* **3**, 1900205 (2020).
5. Oganov, A. R. *et al.* Ionic highpressure form of elemental boron. *Nature* **457**, 863–867 (2009).
6. Albert, B. & Hillebrecht, H. Boron: Elementary challenge for experimenters and theoreticians. *Angew. Chem. Int. Ed.* **48**, 8640–8668 (2009).
7. Thevenot, F. Boron carbide-A comprehensive review. *J. Eur. Ceram. Soc.* **6**, 205–225 (1990).
8. Reddy, K. M., Liu, P., Hirata, A., Fujita, T. & Chen, M. W. Atomic structure of amorphous shear bands in boron carbide. *Nat. Commun.* **4**, 2483 (2013).
9. Barba-Bon, A. *et al.* Boron clusters as broadband membrane carriers. *Nature* **603**, 637–642 (2022).
10. Wang, L. S. Photoelectron spectroscopy of size-selected boron clusters: From planar structures to borophenes and borospherenes. *Int. Rev. Phys. Chem.* **35**, 69–142 (2016).
11. Jian, T. *et al.* Probing the structures and bonding of size-selected boron and doped-boron clusters. *Chem. Soc. Rev.* **48**, 3550–3591 (2019).

12. Bai, H. *et al.* Planar B_{41}^- and B_{42}^- clusters with double-hexagonal vacancies. *Nanoscale* **11**, 23286–23295 (2019).
13. Zhai, H. J. *et al.* Observation of an all-boron fullerene. *Nat. Chem.* **6**, 727–731 (2014).
14. Chen, Q. *et al.* Experimental and theoretical evidence of an axially chiral borospherene. *ACS Nano* **9**, 754–760 (2015).
15. Chen, Q. *et al.* Cage-like B_{41}^+ and B_{42}^{2+}: New chiral members of the borospherene family. *Angew. Chem. Int. Ed.* **54**, 8160–8164 (2015).
16. Chen, Q. *et al.* Endohedral Ca@B_{38}: Stabilization of a B_{38}^{2-} borospherene dianion by metal encapsulation. *Phys. Chem. Chem. Phys.* **18**, 11610–11615 (2016).
17. Tian, W. J. *et al.* Saturn-like charge-transfer complexes Li_4&B_{36}, Li_5&B_{36}^+, and Li_6&B_{36}^{2+}: Exohedral metalloborospherenes with a perfect cage-like B_{36}^{4-} core. *Phys. Chem. Chem. Phys.* **18**, 9922–9926 (2016).
18. Chen, Q. *et al.* Endohedral charge-transfer complex Ga@B_{37}^- : Stabilization of a B_{37}^{3-} borospherene trianion by metal-encapsulation. *Phys. Chem. Chem. Phys.* **18**, 14186–14190 (2016).
19. Chen, W. J. *et al.* B_{48}^-: A bilayer boron cluster. *Nanoscale* **13**, 3868–3876 (2021).
20. Pei, L. *et al.* Bilayer B_{54}, B_{60}, and B_{62} clusters in a universal structural pattern. *Eur. J. Inorg. Chem.* **2020**, 3296–3301 (2020).
21. Yan, Q. Q., Pei, L. & Li, S. D. Predicting bilayer B_{50}, B_{52}, B_{56}, and B_{58}: Structural evolution in bilayer B_{48}–B_{72} clusters. *J. Mol. Model.* **27**, 364 (2021).
22. Pei, L., Yan, Q. Q. & Li, S. D. Predicting the structural transition in medium-sized boron nanoclusters: From bilayer B_{64}, B_{66}, B_{68}, B_{70}, and B_{72} to core-shell B_{74}. *Eur. J. Inorg. Chem.* **2021**, 2618–2624 (2021).
23. Yan, Q. Q. *et al.* A bottom-up approach from medium-sized bilayer boron nanoclusters to bilayer borophene nanomaterials. *Nanoscale* **14**, 1443–1451 (2022).
24. Liu, X. L. *et al.* Borophene synthesis beyond the single-atomic-layer limit. *Nat. Mater.* **21**, 35–40 (2022).
25. Wang, Y. J. *et al.* Observation and characterization of the smallest borospherene, B_{28}^- and B_{28}. *J. Chem. Phys.* **144**, 064307 (2016).
26. Li, H. R. *et al.* Competition between quasi-planar and cage-like structures in the B_{29}^- cluster: Photoelectron spectroscopy and ab initio calculations. *Phys. Chem. Chem. Phys.* **18**, 29147–29155 (2016).
27. Chen, L. B_{14}: An all-boron fullerene. *J. Chem. Phys.* **136**, 104301 (2012).
28. Kiran, B. *et al.* Planar-to-tubular structural transition in boron clusters: B_{20} as the embryo of single-walled boron nanotubes. *PNAS* **102**, 961–964 (2005).
29. Zhao, J. J., Wang, L., Li, F. Y. & Chen, Z. F. B_{80} and other medium sized boron clusters: Core-shell structures, not hollow cages. *J. Phys. Chem. A* **114**, 9969–9972 (2010).
30. Shang, B., Yuan, L. F., Zeng, X. C. & Yang, J. L. Ab initio prediction of amorphous B_{84}. *J. Phys. Chem. A* **114**, 2245–2249 (2010).
31. Li, F. Y. *et al.* B_{80} and $B_{101-103}$ clusters: Remarkable stability of the core-shell structures established by validated density functionals. *J. Chem. Phys.* **136**, 074302 (2012).
32. Prasad, D. L. V. K. & Jemmis, E. D. Stuffing improves the stability of fullerenelike boron clusters. *Phys. Rev. Lett.* **100**, 165504 (2008).
33. Zhang, M., Lu, H. G. & Li, S. D. B_{111}, B_{112}, B_{113}, and B_{114}: The most stable core-shell borospherenes with an icosahedral B_{12} core at the center exhibiting superatomic behaviors. *Nano Res.* **14**, 4719–4724 (2021).
34. Sai, L. W., Wu, X. & Li, F. Y. B_{96}: A complete core–shell structure with high symmetry. *Phys. Chem. Chem. Phys.* **24**, 15687–15690 (2022).
35. Dunk, P. W. *et al.* Formation of heterofullerenes by direct exposure of C_{60} to boron vapor. *Angew. Chem.* **125**, 333–337 (2013).
36. Garg, I., Sharma, H., Dharamvir, K. & Jindal, V. K. Substitutional patterns in boron doped heterofullerenes $C_{60-n}B_n$ (n =1–12). *J. Comput. Theor. Nanos.* **8**, 642–655 (2011).
37. Li, F. Y., Jiang, D. E. & Chen, Z. F. Computational quest for spherical $C_{12}B_{68}$ fullerenes with "magic" pi-electrons and quasi-planar tetra-coordinated carbon. *J. Mol. Model.* **20**, 2085 (2014).
38. Yan, M., Tian, X. X., Pei, L. & Li, S. D. Cage-like $B_{40}C_{30}$, $B_{40}C_{40}$, and $B_{40}C_{50}$: High-symmetry heterofullerenes isovalent with C_{60}, C_{70}, and C_{80}. *J. Mol. Mode.* **24**, 296 (2018).
39. Prasad, D. L. V. K. & Jemmis, E. D. Stuffed fullerenelike boron carbide nanoclusters. *Appl. Phys. Lett.* **96**, 023108 (2010).
40. Nagy, L. G. & Tasi, G. SYVA: A program to analyze symmetry of molecules based on vector algebra. *Comput. Phys. Commun.* **215**, 156–164 (2017).
41. Zhou, T., Lafleur, K. & Caflisch, A. Complementing ultrafast shape recognition with an optical isomerism descriptor. *J. Mol. Graph. Model.* **29**, 443–449 (2010).
42. Ballester, P. J. Ultrafast shape recognition: Method and applications. *Future Med. Chem.* **3**, 65–78 (2011).
43. Grimme, S., Bannwarth, C. & Shushkov, P. A. Robust and accurate tight-binding quantum chemical method for structures, vibrational frequencies, and noncovalent interactions of large molecular systems parametrized for all spd-Block elements (Z = 1–86). *J. Chem. Theory Comput.* **13**, 1989–2009 (2017).
44. Bannwarth, C., Ehlert, S. & Grimme, S. GFN2-xTB-an accurate and broadly parametrized self-consistent tight-binding quantum chemical method with multipole electrostatics and density-dependent dispersion contributions. *J. Chem. Theory Comput.* **15**, 1652–1671 (2019).
45. Vondele, J. V. *et al.* QUICKSTEP: Fast and accurate density functional calculations using a mixed Gaussian and plane waves approach. *Comput. Phys. Commun.* **167**, 103–128 (2005).
46. Adamo, C. & Barone, V. Toward reliable density functional methods without adjustable parameters: The PBE0 model. *J. Chem. Phys.* **110**, 6158–6170 (1999).
47. Tao, J. M. & Perdew, J. P. Climbing the density functional ladder: Nonempirical meta-generalized gradient approximation designed for molecules and solids. *Phys. Rev. Lett.* **91**, 146401 (2003).
48. Feller, D. The role of databases in support of computational chemistry calculation. *J. Comput. Chem.* **17**, 1571–1586 (1996).
49. Frisch, M. J. *Gaussian 09, Revision D.01* (Gaussian Inc. Wallingford, CT, 2009).
50. Glendening, E. D., Landis, C. R. & Weinhold, F. NBO 6.0: Natural bond orbital analysis program. *J. Comput. Chem.* **34**, 1429–1437 (2013).
51. von-Ragué-Schleyer, P., Maerker, C., Dransfeld, A., Jiao, H. J. & van-Eikema-Hommes, N. J. R. Nucleus-independent chemical shifts: A simple and efficient aromaticity probe. *J. Am. Chem. Soc.* **118**, 6317–6318 (1996).
52. Chen, Z. F., Wannere, C. S., Corminboeuf, C., Puchta, R. & von Ragué Schleyer, P. Nucleus-independent chemical shifts (NICS) as an aromaticity criterion. *Chem. Rev.* **105**, 3842–3888 (2005).
53. Zubarev, D. Y. & Boldyrev, A. I. Developing paradigms of chemical bonding: Adaptive natural density partitioning. *Phys. Chem. Chem. Phys.* **10**, 5207–5217 (2008).
54. Tkachenko, N. V. & Boldyrev, A. I. Chemical bonding analysis of excited states using the adaptive natural density partitioning method. *Phys. Chem. Chem. Phys.* **21**, 9590–9596 (2019).
55. Szczepanik, D. W. *et al.* A uniform approach to the description of multicenter bonding. *Phys. Chem. Chem. Phys.* **16**, 20514–20523 (2014).
56. Szczepanik, D. W. *et al.* The electron density of delocalized bonds (EDDB) applied for quantifying aromaticity. *Phys. Chem. Chem. Phys.* **19**, 28970–28981 (2017).
57. Humphrey, W., Dalke, A. & Schulten, K. V. M. D. Visual molecular dynamics. *J. Mol. Graph.* **14**, 33–38 (1996).
58. Wade, K. The structural significance of the number of skeletal bonding electron-pairs in carboranes, the higher boranes and borane anions, and various transition-metal carbonyl cluster compounds. *J. Chem. Soc. D.* **15**, 792–793 (1971).

59. Ciuparu, D., Klie, R. F., Zhu, Y. M. & Pfefferle, L. Synthesis of pure boron single-wall nanotubes. *J. Phys. Chem. B* **108**, 3967–3969 (2004).

Acknowledgements
This work was supported by the National Natural Science Foundation of China (nos. 21720102006 and 21973057 to S.-D. Li and nos. 21473106 to H.-G. Lu).

Author contributions
S.D.L. and H.G.L. designed the project and finalized the manuscript. M.Z., T.Z., B.B.P., and X.T. did the calculations, analyzed the resutls, and prepared the first draft. J.X. and W.P.J. wrote the FMLMS program. All authors reviewed the manuscript.

Competing interests
The authors declare no competing interests.

Additional information
Supplementary Information The online version contains supplementary material available at https://doi.org/10.1038/s41598-022-21809-w.

Correspondence and requests for materials should be addressed to H.-G.L. or S.-D.L.

Reprints and permissions information is available at www.nature.com/reprints.

Publisher's note Springer Nature remains neutral with regard to jurisdictional claims in published maps and institutional affiliations.